



**HAL**  
open science

## Al L<sub>2,3</sub> near edge structure captures the dopant activation and segregation in Al-doped ZnO films

C. Fadel, J. Ghanbaja, S. Migot, S. Cuynet, J.F. Pierson, F. Mücklich, David Horwat

► **To cite this version:**

C. Fadel, J. Ghanbaja, S. Migot, S. Cuynet, J.F. Pierson, et al.. Al L<sub>2,3</sub> near edge structure captures the dopant activation and segregation in Al-doped ZnO films. *Solar Energy Materials and Solar Cells*, 2022, 246, pp.111880. 10.1016/j.solmat.2022.111880 . hal-03813233

**HAL Id: hal-03813233**

**<https://hal.science/hal-03813233>**

Submitted on 14 Oct 2022

**HAL** is a multi-disciplinary open access archive for the deposit and dissemination of scientific research documents, whether they are published or not. The documents may come from teaching and research institutions in France or abroad, or from public or private research centers.

L'archive ouverte pluridisciplinaire **HAL**, est destinée au dépôt et à la diffusion de documents scientifiques de niveau recherche, publiés ou non, émanant des établissements d'enseignement et de recherche français ou étrangers, des laboratoires publics ou privés.

# **Al $L_{2,3}$ near edge structure captures the dopant activation and segregation in Al-doped ZnO films**

C. Fadel<sup>1,2</sup>, J. Ghanbaja<sup>1</sup>, S. Migot<sup>1</sup>, S. Cuynet<sup>1</sup>, J.F. Pierson<sup>1</sup>, F. Mücklich<sup>2</sup>, D. Horwat<sup>1\*</sup>

<sup>1</sup> Université de Lorraine, CNRS, IJL, F-54000 Nancy, France

<sup>2</sup> Department of Materials Science and Engineering, Saarland University, D-66123 Saarbrücken, Germany

\*contact : david.horwat@univ-lorraine.fr

## **Abstract**

Aluminum-doped zinc oxide (AZO) films have been synthesized using reactive high power impulse magnetron sputtering (HiPIMS) in a wide range of Al contents, 0.6-14.7 at.%. The film structure and microstructure investigated by X-ray diffraction and transmission electron microscopy evolves from nanocrystalline columnar film towards ultrafine nanocrystalline films of wurtzite ZnO structure upon increasing the Al content. Electrical properties measured by 4-point probe and Hall effect setups revealed that effective doping maybe achieved up to 3 at.% Al by using HiPIMS. Most importantly, optical transmittance and electronic structure measurements at the Al  $L_{2,3}$  of electron energy loss near edge structure (ELNES) contain signatures of dopant activation, and dopant segregation that may serve to investigate on the origin of electrical properties degradation and to optimize the electrical properties of AZO films.

## **Introduction**

Zinc oxide (ZnO) is a key material for optoelectronics with applications as n-type conductor component of various devices such as oxide solar cells, photodetectors or flat panel displays [1-3]. With a bandgap energy of 3.24 eV, it is highly transparent in the visible range, making it a relevant transparent conductive oxide (TCO), provided proper doping is achieved to reach low electrical resistivity while maintaining the high required transparency [4]. It is considered as a good alternative to the most commonly used TCO indium-doped tin oxide (ITO). ITO may be abandoned as it suffers from the scarcity of indium in the earth crust, high and fluctuating cost, difficulty to recycle and potential toxicity. Doped zinc oxide is a prioritized alternative owing to its performance as well as the abundance, low cost, low toxicity and good recyclability of its constituting elements. It is usually doped with group III elements such as Al, in order to achieve low resistivity. However, under stable thermodynamic conditions, the solubility limit of Al in ZnO is quite low at around 0.3 at% [5]. To reach high active dopant concentrations in ZnO

films, the films need to be grown using a non-equilibrium method such as physical vapor deposition (PVD) [6]. Yet, the optimum extrinsic dopant concentration is not clearly defined to date and is highly dependent on the synthesis conditions. More precisely, the performance of Al-doped zinc oxide (AZO) thin films, and TCO in general, results from a compromise between optical and electrical properties and a complex interplay between intrinsic and extrinsic doping, compensation of dopants and different contributions to free electron scattering [7-9]. While various studies have attempted to correlate electronic structure measurements to the actual doping of AZO, the results were often subject to caution and discussions [10-16] and an appropriate method to detect signs of dopant activation in the electronic structure is still to be found. In the present study we evaluate the influence of the Al content on optical, electrical, microstructural properties of AZO thin films and correlate it with electronic structure modifications as probed by electron energy loss near edge structure (ELNES) at the Zn-L<sub>3</sub> and Al-L<sub>2,3</sub> edges. It is shown in particular that the Al-L<sub>2,3</sub> edges contain the signature for effective extrinsic doping by Al below 3at.% Al and progressive deactivation of Al dopant by placement into octahedral conformation at higher Al contents.

### **Experimental methods**

Thin AZO films were synthesized using reactive high power impulse magnetron sputtering (R-HiPIMS) of Zn-Al targets provided by HMW and containing 1,2, 5, 10 and 15 at.% Al, following the procedure first reported in [17] for a 3 at.% Al target. Details of the geometry of experimental setup can be found in the figure S1 of supplementary materials. The experimental device was a 40-L sputtering chamber pumped down via a primary and a secondary pumps in order to achieve 10<sup>-5</sup> mbar before deposition. The pressure was monitored by a Leybold CERAVAC CTR100N vacuum transmitter. The argon and oxygen gas mixtures were fed into the chamber via the Bronkhorst FlowView 2V1.23 software and Bronkhorst High-Tech flowmeters.

The distance between target and the substrate-holder was of 8 cm with both surfaces parallel. The distance between the target axis and the rotating substrate-holder rotation axis was of 8 cm. Soda lime glass samples were placed radially allowing to characterize film properties at different radial positions. Film properties were measured after a first screening of the electrical properties. They were collected at 3 cm from the substrate-holder axis, leading to films of low resistivity, and at the position leading to the highest electrical resistivity, usually at or close to the position facing the target axis (8 cm from the substrate-holder axis).

The targets were mounted on a type II NdFeB unbalanced magnetron and were supplied with an Advanced Energy<sup>®</sup> MDX 500 DC power supply used for target surface cleaning in order to remove surface oxide layer. The applied etching current was 0.1 A for all targets, 50 sccm of Argon were injected and the etching time varied between 15 and 30 mins. Target cleaning was considered completed as the target voltage reached an asymptotic voltage value. Once the etching was done, the targets were then supplied by a MELEC GmbH Spik 2000A HiPIMS generator which in itself was charged by an Advanced Energy<sup>®</sup> Pinnacle Plus 5 kW operated in DC mode. A negative unipolar mode with a 100  $\mu$ s time on and 900  $\mu$ s time off (10% duty cycle) was applied and the discharge voltage was tuned by the Pinnacle Plus generator in the 400 to 600 V range. The resulting current was monitored by a Pearson<sup>™</sup> Current Monitor probe (output V/A = 0.1) and the applied voltage to the target was monitored by a Cal Test CT4028 High Voltage divider probe with an accuracy of  $\leq 3\%$ ; the pulse current and the voltage were observed on a Tektronix TDS 2024B oscilloscope (200 MHz bandwidth and 2 GS/s maximum sample rate). All depositions lasted 40 min and the flow rate of argon was always set to 80 sccm in all cases, in order to reach a deposition pressure close to 1 Pa. The discharge voltage and oxygen flow rate were set after a series of depositions leading to films with the lowest possible resistivity while maintaining optical transparency. No thermal assistance was used during deposition. Optical transmittance was measured using a Carry 5000 spectrophotometer and served to calculate the absorption coefficient and extract optical bandgap using the Tauc approach. The crystal structure was analyzed using a Brücker D8 Advance diffractometer with a Cu  $K_{\alpha}$  radiation and details of the microstructure were obtained using a high resolution scanning/transmission electron microscope. A Jeol JEM - ARM 200F Cold FEG TEM/STEM operating at 200 kV and equipped with a spherical aberration (Cs) probe and image correctors (point resolution 0.12 nm in TEM mode and 0.078 nm in STEM mode) was used. TEM lamellae were prepared by FIB from the deposited AZO films using a FEI Helios Nanolab 600i focused ion beam scanning electron microscope (FIB-SEM). High resolution-TEM (HR-TEM) images and selected area electron diffraction (SAED) patterns were obtained in TEM mode. The STEM mode enabled to perform energy dispersive spectroscopy (EDS) in order to extract the film Al content. Moreover, electron energy loss near edge structure (ELNES) was collected at Al-L<sub>2,3</sub> and Zn-L<sub>3</sub> edges. The electrical resistivity was measured using a 4-point probe setup connected to a Keithley 237 voltage source and a Keithley 2700 multimeter. The mobility and charge carrier density were measured on selected samples using a HMS 5000 Hall effect measurement setup from Ecopia.

## Results

We first analyze the evolution of the electrical resistivity as a function of sample position relative to the substrate-holder axis and target composition. Both parameters have a sensitive influence on the electrical resistivity : Increasing the target composition from 1 to 10 at% Al in the target increases the resistivity except for position 3 cm deposited using the 2 at% Al target, and the resistivity tends to increase as approaching from the target axis. These results are consistent with previous reports indicating that lowest resistivity is achieved at low Al contents [18, 19] and bombardment by fast particles emitted perpendicular to the target surface degrades the film electrical performance [17, 20, 21]. For further analysis, films located at 3 cm from the substrate-holder, labelled as “low  $\rho$ ”, and at the position corresponding to the highest resistivity, labelled as “high  $\rho$ ” as indicated by arrows in figure 1. All films synthesized using the 15 at% Al target were too insulating to be measured using our 4-point probe setup. Yet, 3 and 8 cm positions were also selected for further analysis of films synthesized from the 15 at.% Al Zn-Al target.

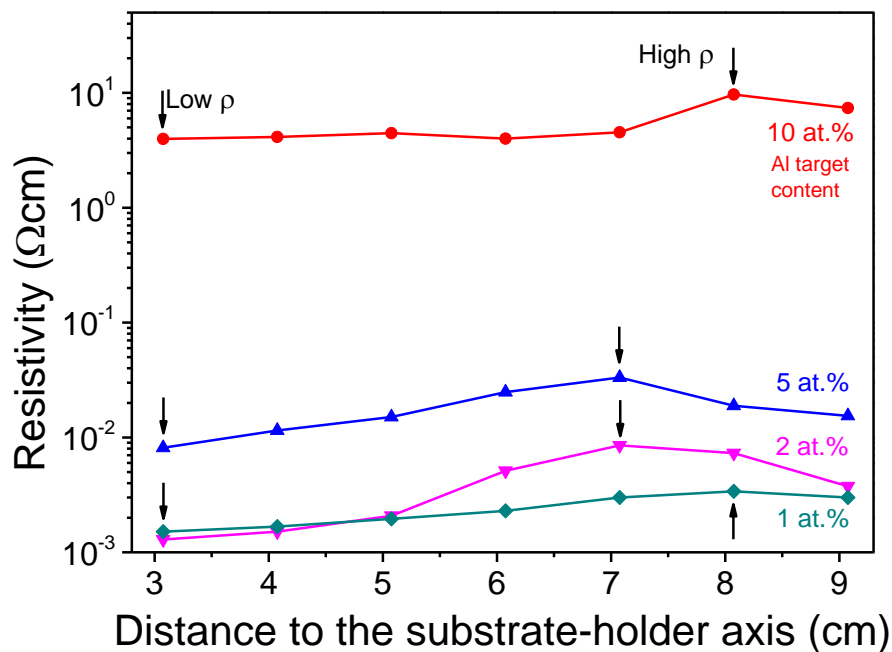


Figure 1 : Evolution of the electrical resistivity with sample position relative to the rotation axis of the substrate-holder for films deposited using Zn-Al targets of different Al contents. The target axis was located at 8 cm from the substrate-holder axis. Arrows indicate the positions representative of low/high resistivity and used for further analysis. Films deposited using the

15 at.% Al target were too resistive to be measured, but for this position also 3 and 8 cm positions were selected for further analysis.

Table I reports the film composition and electrical properties measured at the low and high resistivity positions using the five different targets along with the average size crystallites derived from XRD or TEM analysis. It is verified that increasing the Al content in the target leads to increase in the Al content in the coatings, as measured by EDS on TEM lamellae extracted from the deposited films. Yet, slight variations are observed depending on high or low resistivity positions. These variations can arise due to changes in the spatial distribution of sputtered atoms that is different for each element and discharge parameters, their transport affected by collisions with the background gas and relative sticking probability to the surface of the growing film. We observed that the increase in resistivity is associated to decrease in both electron density and electron mobility for resistivity in the  $10^{-3}$   $\Omega$  cm range leading to relevant data with our measurement setup. In this range, no clear correlation of the electrical resistivity to the size of crystallites is found. This is consistent with the fact that electrons are little sensitive to grain boundary scattering but rather to ionized impurity scattering when the electron density is high [9]. For higher resistivity values, it was not possible to measure the electron density and electron mobility using our experimental setup.

Table I : Al content, electrical properties and average size of crystallites measured at high and low resistivity positions for films deposited using targets of various Al contents. <sup>a</sup>Average size of crystallites for 15 at.% Al was deduced from TEM analysis while XRD was used to evaluate the size of crystallites for other conditions. NM : non-measurable.

Target composition	Film composition (at. % Al)	Resistivity ( $\Omega$ .cm)	Electron density ( $\text{cm}^{-3}$ )	Electron mobility ( $\text{cm}^2\text{V}^{-1}\text{s}^{-1}$ )	Average size of crystallites (nm)
			<i>high / low resistivity</i>		
1 at. % Al	0.6 / 0.7	$3.4 \cdot 10^{-3} / 1.5 \cdot 10^{-3}$	$7.3 \cdot 10^{20} / 1.2 \cdot 10^{21}$	3.7 / 5.1	27 / 27
2 at.% Al	0.9 / 1.0	$8.5 \cdot 10^{-3} / 1.3 \cdot 10^{-3}$	$3.5 \cdot 10^{20} / 1.9 \cdot 10^{21}$	3.0 / 4.7	30 / 25
5 at.% Al	2.9 / 1.9	$3.3 \cdot 10^{-2} / 8.1 \cdot 10^{-3}$	NM / $5.0 \cdot 10^{19}$	NM / 0.4	12 / 16
10 at.% Al	6.2 / 7.0	9.68 / 3.98	NM / NM	NM / NM	$\sim 5 \text{ nm}^a$
15 at.% Al	14.7 / 12.1	NM	NM / NM	NM / NM	$\sim 4 \text{ nm}^a$

Microstructural analysis was conducted using XRD and TEM. The X-ray diffractograms of figure 2 correspond the diffracted intensity normalized by the film thickness. They show similar evolution with the Al content for high and low resistivity conditions. It is found that the diffraction signal for Al contents below or equal to 7 at.% Al is consistent with the hexagonal

wurtzite structure of ZnO. Multiple orientations are clearly distinguished below 3 at. % Al in the films. This has been linked to oxygen sub-stoichiometry in previous reports [7, 17]. Increasing the Al content in the films to around 6-7 at. % Al, the diffractograms exhibit a broad peak corresponding to diffraction by (002) planes of hexagonal wurtzite ZnO. Finally, the diffracted signal corresponds to amorphous or ultrafine nanocrystalline films above 12 at. % Al.

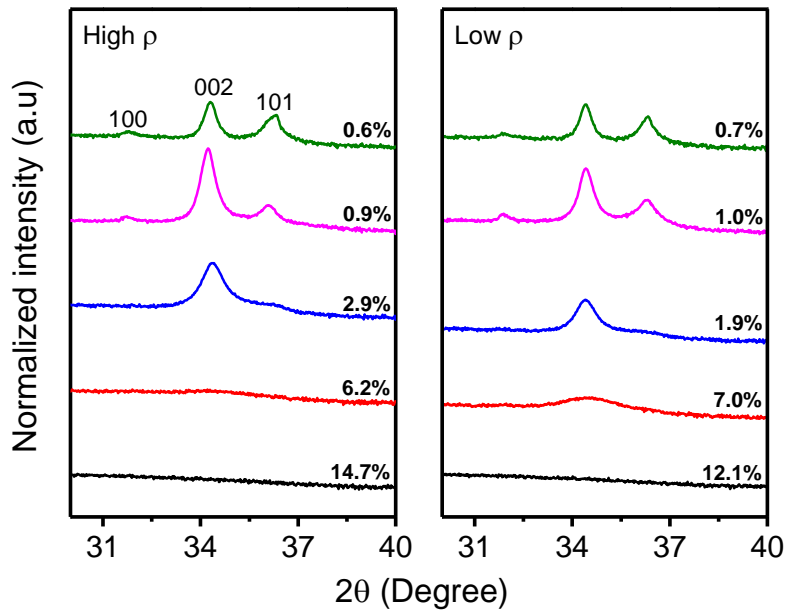


Figure 2 : X-ray diffractograms of films corresponding to high/low resistivity conditions as defined from figure 1. The diffraction planes indicated correspond to hexagonal wurtzite ZnO structure.

TEM analysis was conducted on all samples in order to gain further details on the microstructure. Figure 3 shows the HRTEM images and corresponding FFT pattern of samples containing 6.2 and 14.7 at.% Al. Despite the very weak signal observed in the XRD diffractogram of those films, they are found nanocrystalline with a size of crystallites close to 5 nm. The FFT patterns evidence that they exhibit the crystal structure of hexagonal wurtzite ZnO. Therefore, incorporation of Aluminum into ZnO can maintain the crystalline structure with the amounts used within this study.

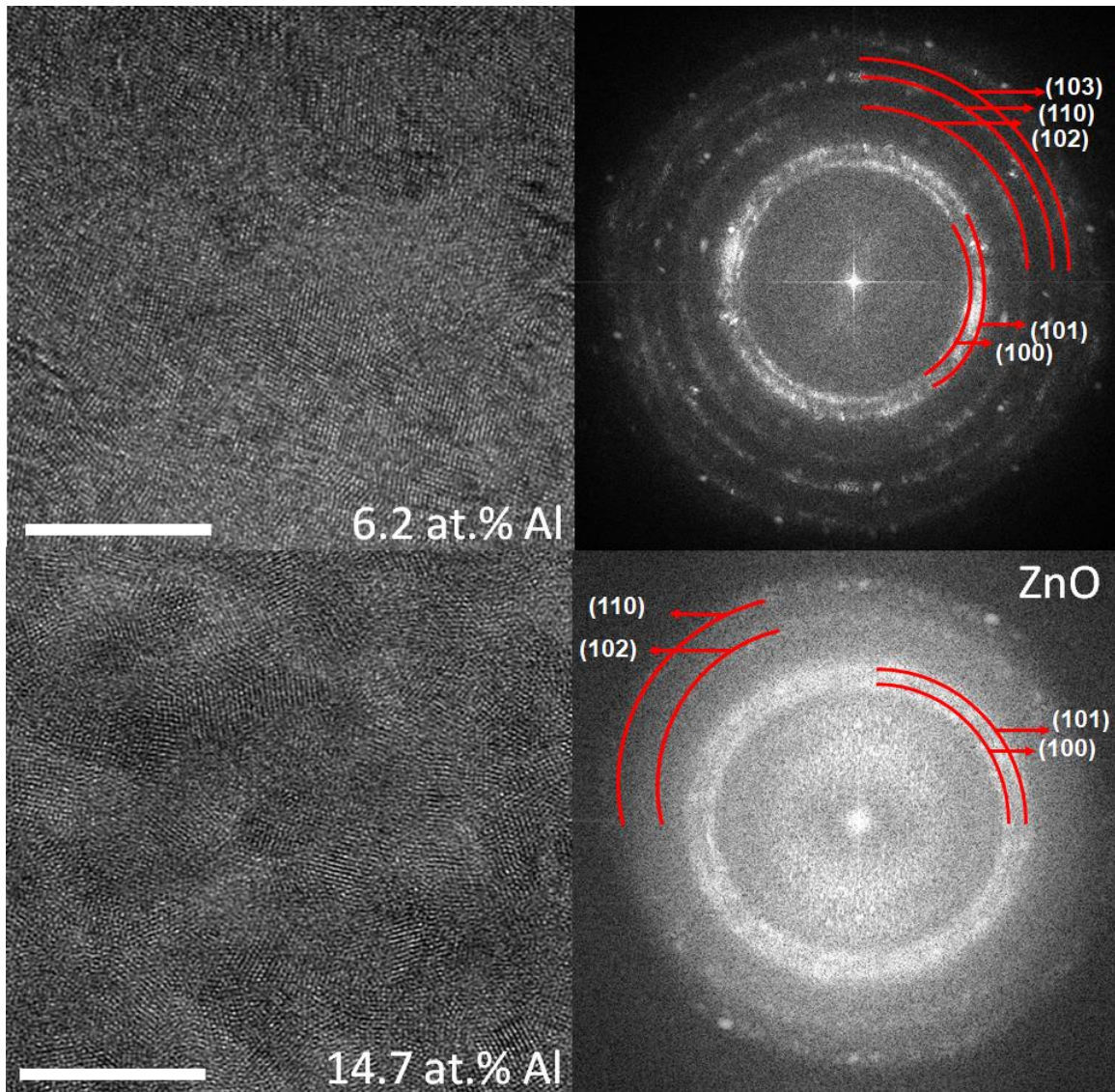


Figure 3 : HRTEM of 6.2 and 14.7 at.% Al ZnO films and corresponding FFT patterns. The scale bar represents 10 nm. Table 2 summarizes the main results derived from optical measurements in terms of transmittance and optical bandgap. The transmittance is generally high in the visible range. Yet, lower values are found for the films with Al contents equal or below 1 at.% Al. Lower transmittance is also a signature for lower oxygen content in the films [7, 17].

Table II : Al content and optical properties measured at high and low resistivity positions for films deposited using targets of various Al contents.

Target composition	Film composition (at. % Al)	Average visible transmittance (%)	Bandgap (eV)
<i>high / low resistivity</i>			
1 at. % Al	0.6 / 0.7	76 / 61	3.49 / 3.56
2 at.% Al	0.9 / 1.0	87 / 76	3.46 / 3.72
5 at.% Al	2.9 / 1.9	87 / 89	3.50 / 3.56
10 at.% Al	6.2 / 7.0	83 / 91	3.90 / 3.86
15 at.% Al	14.7 / 12.1	89 / 89	4.22 / 4.17

The Tauc plots of figure 4 enabled to extract the optical bandgap for the different compositions and positions. Transmittance curves are available as supplementary material (Figure S2). Noteworthy, the optical bandgap is higher than 3.24 eV expected for undoped ZnO. For highly conductive films of high electron densities above the Mott density, of typically  $10^{18} \text{ cm}^{-3}$  [22], the bandgap value is in the 3.46 – 3.72 eV range. This increase in bandgap is explained by the Burstein-Moss effect [23] as the fermi level is shifted in the conduction band. For high Al contents, resistivity values are not consistent with Burstein-Moss effect as the electrical conductivity is poor or even not measurable. Hence, the large bandgap for the coatings of Al contents higher than 3 at.% may rather reflect a chemical effect.

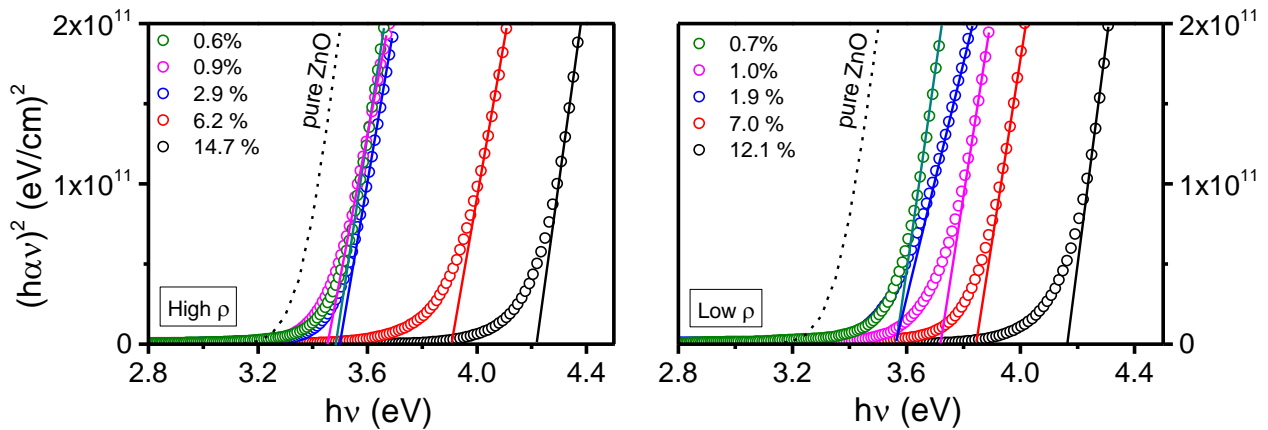


Figure 4 : Tauc plots for films corresponding to high/low resistivity conditions as defined in figure 1 and for pure ZnO.

Figure 5 illustrates how the bandgap is affected by the chemical composition. For the lowest Al content there is no comprehensive evolution with the Al content but rather an effect of the electron density. In contrast, from 3 at.% Al, the bandgap monotonously increases with the Al content. This change might result from a progressive change in the bonding as more aluminum is incorporated into ZnO.

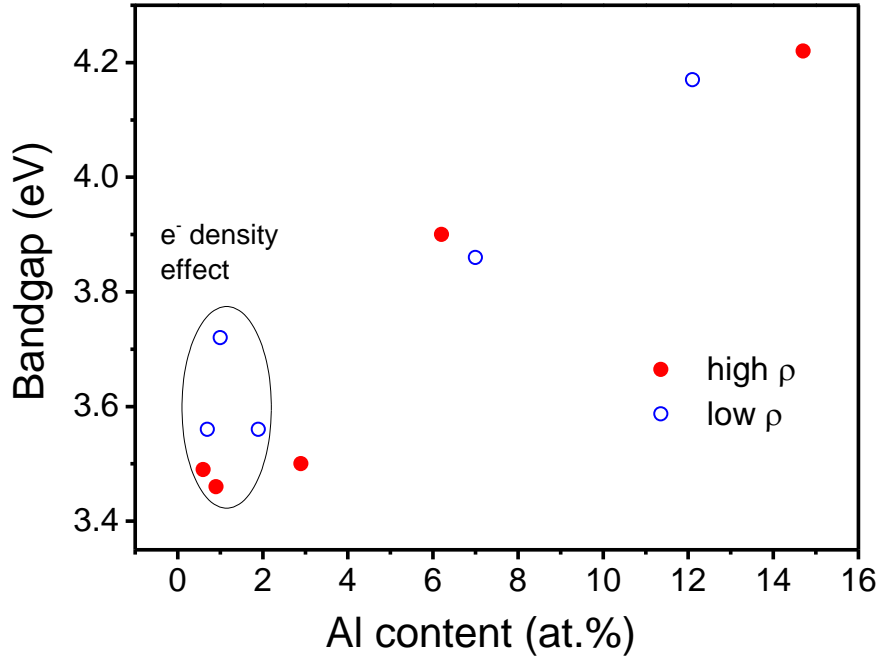


Figure 5 : Evolution of the optical bandgap as a function of the Al content incorporated into ZnO.

The segregation of aluminum in sputter-deposited ZnO thin films has already been reported to lead to formation of alumina,  $\text{Al}_2\text{O}_3$ , but for Al contents higher than 30 at. % and using thermal assistance of 400 °C during deposition [24]. While the optical bandgap of bulk crystalline  $\text{Al}_2\text{O}_3$  is between 7 and 8.8 eV, it decreases to 5.1 to 7.1 eV for amorphous  $\text{Al}_2\text{O}_3$  and between 3.2 and 6.2 eV in thin films form [25, 26]. The stable secondary phase forming above the solubility limit of Al in ZnO is spinel  $\text{ZnAl}_2\text{O}_4$  in which aluminum adopts an octahedral conformation with oxygen, but Bikowski et al. [15] have not found indication of its formation in the O-K, Zn-L and Al-K edges X-ray absorption near edge structure (XANES) of films containing approximately 2 at. % Al, even for deposition temperatures as high as 500 °C. The optical bandgap of  $\text{ZnAl}_2\text{O}_4$  can be tuned between 3.9 and 6 eV in nanocrystalline phase [27-29]. Another possibility proposed by Yoshioka [11] is the formation of homologous  $\text{Al}_2\text{O}_3(\text{ZnO})_m$  phases. Such structures can schematically be regarded as nanolaminates of poorly-doped ZnO blocks, with Al in tetrahedral and pentahedral conformations, alternating along the c-axis with  $\text{Al}_2\text{O}_3$ -like monolayers of octahedral conformation with oxygen. Variations of the Al-K edge XANES by Yoshioka et al. [10-11], Vinnichenko et al. [14 ], Horwat et al. [12, 13] were claimed to be consistent with homologous structure formation in AZO films. More recently, Rijpstra et al. proposed, using an evolution algorithm, the more energetically-favorable

formation of another phase of structure very close to the homologous phases but instead of the nanolaminated homologous phase, this structure can be characterized as separate  $\text{Al}_2\text{O}_3$ -threads woven into a ZnO medium [16]. In contrast to secondary phase formation, Bikowski et al. interpreted small changes at the Al-K edge by the formation of  $\text{Al}_{\text{Zn}}\text{-O}_i$  complexes [15]. Unfortunately, direct evidence of the formation of such structures or complexes is not available to date: The XRD signature of their formations is not easily distinguishable from the signal of wurtzite ZnO or in previous electronic structure measurements and, to date, there is no TEM analysis proving it. As a consequence, the mechanisms behind the deactivation of the Al dopant in AZO films remain unsolved. In order to try to solve it, we propose in the following an alternative tool based on direct detection of active Al dopant, and transition from active to inactive Al, in electronic structure measurements.

Figure 5 displays the Zn  $L_3$  ELNES of AZO films for high resistivity and low resistivity conditions. This edge corresponds to transition of electrons from Zn  $2p_{3/2}$  to Zn s- and d-derived empty states. Since the Zn 3d orbital is fully occupied, this edge probes the density of unoccupied Zn 4s and Zn 4d states with some overlap with other orbitals. 4 distinct features noted  $A_{\text{Zn-L}}$ ,  $B_{\text{Zn-L}}$ ,  $C_{\text{Zn-L}}$  and  $D_{\text{Zn-L}}$  are observed. Feature  $A_{\text{Zn-L}}$  reflects the density of Zn 4s states, features  $B_{\text{Zn-L}}$  is a combination of Zn 4s and Zn 4d states, while  $C_{\text{Zn-L}}$  and  $D_{\text{Zn-L}}$  are ascribed to Zn 4d states [30, 31]. The ELNES of films deposited containing up to 2.9 at.% Al exhibits spectral shape typical of wurtzite ZnO, despite small variations in the intensity of feature  $A_{\text{Zn-L}}$ . For higher Al contents, features  $B_{\text{Zn-L}}$ ,  $C_{\text{Zn-L}}$  and  $D_{\text{Zn-L}}$  become weaker and smeared out, possibly due to weakening of the film crystallinity and changes in the Zn 4s and Zn 4d overlap with oxygen due to local crystal distortions [31]. Interestingly, the film deposited in low resistivity position and containing 7.0 at.% Al still presents detectable distinct features and the XRD analysis revealed the presence of the (002) diffraction peak (see figure 2). In contrast, the film of close composition (6.2 at.%) and deposited under high resistivity position exhibits less defined features in the ELNES as well as a weaker (002) diffraction peak. Feature  $A_{\text{Zn-L}}$  gives information on the Zn 4s states, corresponding to the bottom of the conduction band. It tends to increase as the Al content reaches 1.9 at% and beyond, indicating progressive emptying of these states.

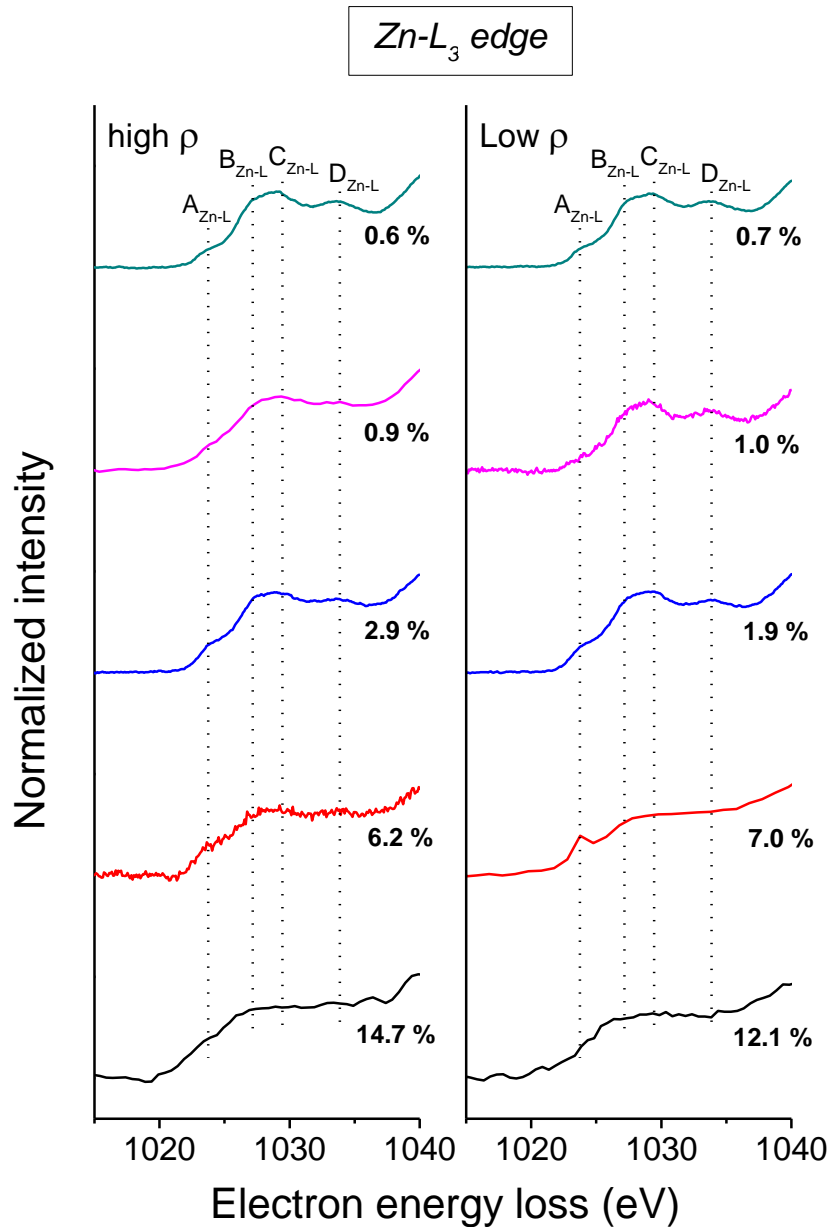


Figure 5 : Zn  $L_3$  electron energy loss near edge structure of the films corresponding to high/low resistivity conditions as defined in figure 1.

The Al- $L_{2,3}$  edges ELNES of our AZO films is shown in figure 6. This edge corresponds to the transition from Al  $2p_{3/2}$  ( $L_3$  edge) and Al  $2p_{1/2}$  ( $L_2$  edge) electrons to Al s- and d-derived states. The  $L_3$  and  $L_2$  edges corresponds to the signal below and above approx. 105 eV, respectively.

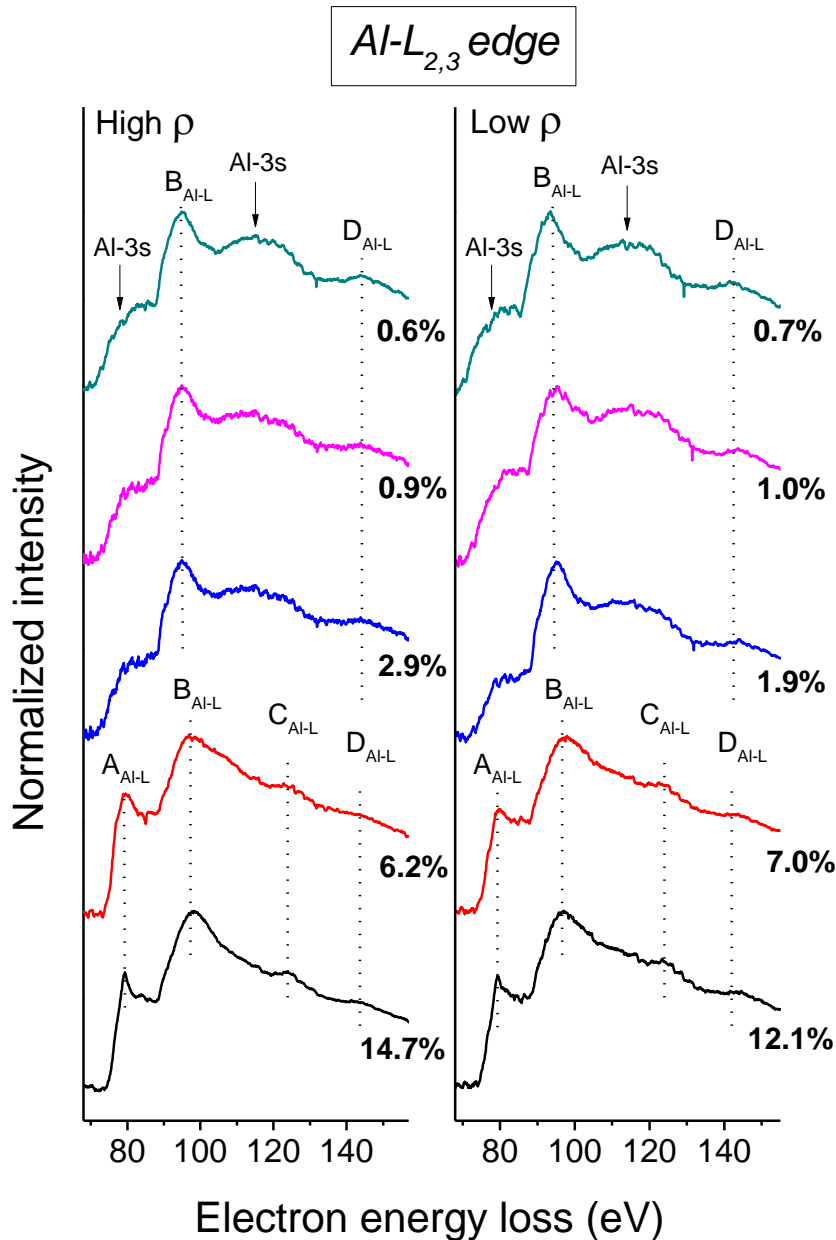


Figure 6 :  $Al L_{2,3}$  electron energy loss near edge structure of the films corresponding to high/low resistivity conditions as defined in figure 1.

Contributions at the  $L_2$  edge are broadened and weak replicas of the  $L_3$  edge contributions. The spectra for films containing 2.9 at. % Al or less are characterized by a wide signal at the bottom of both edges. To the best of our knowledge, this signal has not been reported for Aluminum in tetrahedral or octahedral conformation in minerals and it may be a specific feature of active aluminum. Interestingly, Imai et al. have shown using DFT that electron conduction in Al-doped ZnO results from a highly delocalized Al 3s state that appears near the fermi level close

to the conduction band minimum [32]. Wang et al. have obtained similar results [33]. Interestingly, the observed broad features in the ELNES of samples containing less than 2.9 at. % Al reproduce well the broad Al 3s density of empty states in the conduction band calculated in [32]. Moreover, the shape of feature  $B_{Al-L}$  of these samples is in agreement with tetrahedral aluminum [34], corresponding to the substitution of Zn by Al, i.e. the active conformation of aluminum in ZnO. Therefore, the presence of a broad Al-3s contributions in the Al-L<sub>2,3</sub> ELNES may be used as a sensitive tool to probe efficient doping of ZnO by Al. The ELNES spectral shape for films of 6.2 at.% Al and higher contents is very different. It exhibits the usual narrow feature  $A_{Al-L}$  of Al in minerals, accounting for more localized states in more resistive materials. It is not easy to distinguish between the ELNES spectra of tetrahedral and octahedral aluminum. Yet, the broadening of feature  $B_{Al-L}$  and the single-peaked contribution  $A_{Al-L}$  is in favor for the presence of octahedral aluminum [34]. Looking more carefully to samples containing 6.2 and 7.0 at.% Al we find that the  $A_{Al-L}$  feature is less peaked than in the richest samples and slight humps are observed at the left and right of feature  $A_{Al-L}$  and  $B_{Al-L}$ , respectively. This suggests that the spectra for these samples, and eventually samples richer in Aluminum, might be composed by the convolution of active and inactive signals of aluminum. In order to verify this assumption, we have modelled the ELNES of the film containing 7.0 % Al by mixing the reference ELNES spectra of active Al (0.6 at.% Al) with that of inactive aluminum. The later was constructed by assuming a possible overlap of the signal of inactive (supposedly octahedral) aluminum with that of active Al in the ELNES of the 14.2 At.% Al sample, by attempting to maximize the peak intensity of the  $A_{Al-L}$  and the bump at the right side of  $B_{Al-L}$ . Figure 7 shows the obtained results considering that the signal for 14.2 at. % Al is composed by 70 mol. % of inactive Al and 30 mol.% active tetrahedral Al. Moreover, the ELNES spectral shape for 7 at.% Al is well reproduced considering the mixing of 55 mol.% of inactive Al and 45 mol.% active Al. Despite spectral broadening of the  $A_{Al-L}$  contribution is not perfectly reproduced, our model appears to reproduce the progressive inactivation of aluminum as the Al content is increased and as resistivity increases. It could therefore be used in future studies to evaluate the actual solubility of Al into the wurtzite structure of ZnO and activation/deactivation of the Al dopant in far out of stable equilibrium conditions. Moreover, presented results indicate that using far out of stable equilibrium methods such as reactive HiPIMS, it is possible to solubilize nearly 3 at.% Al into wurtzite ZnO. Nevertheless, optical data indicate that some of the Al atoms present in the 0.6 and 0.7 at.% Al films are likely segregated. Therefore, a limitation of our model is to consider the Al-L<sub>2,3</sub> edges ELNES of 0.6 at.% Al as a reference for perfectly activated Al and future studies may refine this model.

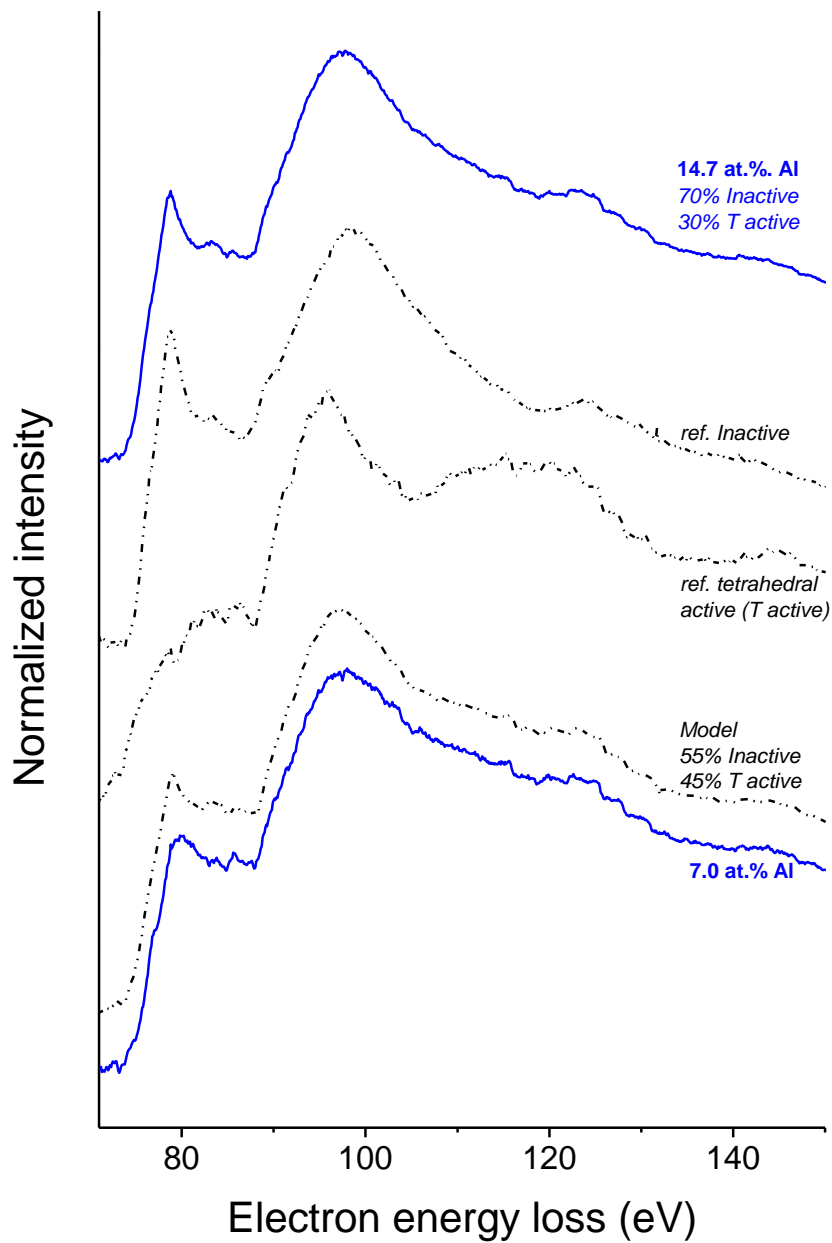


Figure 7 : Al  $L_{2,3}$  edge reference spectra for electrically Inactive and active Al serving as a basis to extract the proportions of inactive and active Al.

## Conclusion

Thin films of aluminum-doped zinc oxide (AZO) were deposited using reactive high power impulse magnetron sputtering (R-HiPIMS) in a wide range of Al contents, from 0.6 to 14.7 at.%. Presented results indicate that R-HiPIMS is suitable to achieve high conductivity without

thermal assistance up to an Al content of 3 at.%. Above this threshold, significant degradation of the electrical properties is observed. A likely mechanism for such degradation is the segregation of aluminum in inactive conformation with oxygen, most likely in octahedral conformation. As a consequence, two optical bandgaps can be detected from optical transmittance measurements, the higher one corresponding to nanoscale segregation in inactive conformation. Additionally, we found that electronic structure measurements at the Al<sub>2,3</sub> electron energy loss near edge structure (ELNES) are highly sensitive to changes in the Al conformation and can capture the activation/deactivation of the Al dopant. Therefore, modelling of the Al<sub>2,3</sub> ELNES can serve as a platform to unravel the mechanisms behind the degradation of, and to optimize, the electrical properties of bulk and thin film AZO.

### **Acknowledgments**

The authors acknowledge financial support from INTERREG project PULSATEC and French Ministère de l'Enseignement Supérieur et de la Recherche for the funding of CF PhD thesis. CF acknowledges support from German-French University for help with accommodation and travel expenses within the PhD-Track project "German-French Graduate School in Materials Science and Engineering".

### **Author contributions**

CF Performed the depositions, optical, electrical and X-ray diffraction analyses, prepared figures, participated to manuscript writing and editing. DH designed the experiments, prepared figures, participated to manuscript writing, editing and reviewing, secured part of funding. SC designed the experiments and participated to manuscript reviewing. SM extracted the FIB foils, participated to manuscript reviewing. JG conducted the TEM measurements, participated to manuscript reviewing. JFP and FM secured the main part of funding, participated to manuscript reviewing

### **References**

- [1] T. Minami, Y. Nishi, T. Miyata, J. Nomoto, High-Efficiency Oxide Solar Cells with ZnO/Cu<sub>2</sub>O Heterojunction Fabricated on Thermally Oxidized Cu<sub>2</sub>O Sheets, Appl. Phys. Express 4 (2011) 062301
- [2] C. de Melo, M. Jullien, Y. Battie, A. En Naciri, J. Ghanbaja, F. Montaigne, J-F. Pierson, F. Rigoni, N. Almqvist, A. Vomiero, S. Migot, F. Mücklich, D. Horwat, Semi-Transparent

p-Cu<sub>2</sub>O/n-ZnO Nanoscale-Film Heterojunctions for Photodetection and Photovoltaic Applications, *ACS Appl. Nano Mater.* 2019, 2, 4358–4366, DOI: 10.1021/acsnm.9b00808

[3] L. Qian, Y. Zheng, J. Xue, P.H. Holloway, Stable and efficient quantum-dot light-emitting diodes based on solution-processed multilayer structures. *Nat. Photon.* 5 (2011) 543–548

[4] W. Beyer, J. Hüpkes, H. Stiebig, Transparent conducting oxide films for thin film silicon photovoltaics, *Thin Solid Films* 516 (2–4) (2007)147–154,  
<http://dx.doi.org/10.1016/j.tsf.2007.08.110>.

[5] K. Shirouzu, T. Ohkusa, M. Hotta, N. Enomoto, J. Hojo, Distribution and Solubility Limit of Al in Al<sub>2</sub>O<sub>3</sub>-Doped ZnO Sintered Body, *J. Ceram. Soc. Jpn.* 115 (1340) (2007) 254–258, doi:10.2109/jcersj.115.254.

[6] A. Zakutayev, N. H. Perry, T. O. Mason, D. S. Ginley, S. Lany, Nonequilibrium origin of high electrical conductivity in gallium zinc oxide thin films, *Appl. Phys. Lett.* 103 (23) (2013) 232106, doi:10.1063/1.4841355

[7] M. Jullien, D. Horwat, F. Manzeh, R. Escobar Galindo, Ph. Bauer, J.F. Pierson, J.L. Endrino, *Sol. Energy Mater. Sol. Cells* 95 (2011) 2341–2346, doi:10.1016/j.solmat.2011.04.003, doi : 10.1016/j.solmat.2011.04.003

[8] S. Cornelius, M. Vinnichenko, N. Shevchenko, A. Rogozin, A. Kolitsch, W. Möller, Achieving high free electron mobility in ZnO:Al thin films grown by reactive pulsed magnetron sputtering. *Appl. Phys. Lett.* 94 (2009) 042103

[9] A. Bikowski, K. Ellmer, Analytical model of electron transport in polycrystalline, degenerately doped ZnO films, *J. Appl. Phys.* 116 (2014) 143704, doi: 10.1063/1.4896839

[10] S. Yoshioka, K. Toyoura, F. Oba, A. Kuwabara, K. Matsunaga, I. Tanaka, First-principles investigation of R<sub>2</sub>O<sub>3</sub>(ZnO)<sub>3</sub> (R=Al, Ga, and In) in homologous series of compounds, *J. Solid State Chem.* 181 (2008) 137-14

[11] S. Yoshioka, F. Oba, R. Huang, I. Tanaka, T. Mizoguchi, T. Yamamoto, Atomic structures of supersaturated ZnO – Al<sub>2</sub>O<sub>3</sub> solid solutions, *J. Appl. Phys.* 103 (2008) 014309, doi : 10.1063/1.2829785

[12] D. Horwat, M. Jullien, F. Capon, J-F. Pierson, J. Andersson, J.L. Endrino, On the deactivation of the dopant and electronic structure in reactively sputtered transparent Al-doped ZnO thin films, *J. Phys. D : Appl. Phys.* 43 (2010) 132003, doi: 10.1088/0022-3727/43/13/132003

[13] D. Horwat, M. Mickan, W. Chamorro, New strategies for the synthesis of ZnO and Al-doped ZnO films by reactive magnetron sputtering at room temperature, *Phys. Stat. Sol. C* 13 (2016) 951-957, doi: 10.1002/pssc.201600136

[14] M. Vinnichenko, R. Gago, S. Cornelius, N. Shevchenko, A. Rogozin, A. Kolitsch, F. Munnik, W. Möller, Establishing the mechanism of thermally induced degradation of ZnO:Al electrical properties using synchrotron radiation, *Appl. Phys. Lett.* 96 (2010) 141907, doi: 10.1063/1.3385024

- [15] A. Bikowski, D. A. Zajac, M. Vinnichenko, K. Ellmer, Evidence for the  $\text{Al}_{\text{Zn}}\text{-O}_i$  defect-complex model for magnetron-sputtered aluminum doped zinc oxide: A combined X-ray absorption near edge spectroscopy, X-ray diffraction and electronic transport study, *J. Appl. Phys.* 126 (2019) 045106, <https://doi.org/10.1063/1.5089555>
- [16] K. Rijpstra, S. Cottenier, M. Waroquiera, V. Van Speybroeck, Crystal structure prediction for supersaturated AZO: the case of  $\text{Zn}_3\text{Al}_2\text{O}_6$ , *Cryst. Eng. Comm.* 15 (2013) 10440–10444, doi: 10.1039/c3ce41009a
- [17] M. Mickan, U. Helmersson, H. Rinnert, J. Ghanbaja, D. Muller, D. Horwat, Room temperature deposition of homogeneous, highly transparent and conductive Al-doped ZnO films by reactive high power impulse magnetron sputtering, *Sol. Energy Mater. Sol. Cells* 157 (2016) 742-749, doi: 10.1016/j.solmat.2016.07.020
- [18] B. Paul, B. Singh, S. Ghosh, A. Roy, A comparative study on electrical and optical properties of group III (Al, Ga, In) doped ZnO, *Thin Solid Films* 603 (2016) 21-28, doi: 10.1016/j.tsf.2016.01.044
- [19] A. K. Das, P. Misra, R. S. Ajimsha, A. Bose, S. C. Joshi, D. M. Phase, L. M. Kukreja. Metal to semiconductor transition in lightly Al doped ZnO thin films grown by sequential pulsed laser deposition, *J. Appl. Phys.* 112, (2012) 103706, <https://doi.org/10.1063/1.4765733>
- [20] A. Bikowski, T. Weltzel, K. Ellmer, The correlation between the radial distribution of high-energetic ions and the structural as well as electrical properties of magnetron sputtered ZnO:Al films, *J. Appl. Phys.* 114 (2013) 223716 (2013), <https://doi.org/10.1063/1.4840975>
- [21] E. Stamate, Spatially Resolved Optoelectronic Properties of Al-Doped Zinc Oxide Thin Films Deposited by Radio-Frequency Magnetron Plasma Sputtering Without Substrate Heating, *Nanomaterials* 10 (2020) 14, doi: doi:10.3390/nano10010014
- [22] M. A. M. Versteegh, T. Kuis, H. T. C. Stoof, J. I. Dijkhuis, Ultrafast screening and carrier dynamics in ZnO: Theory and experiment, *Phys. rev. B*, 84 (2011) 035207, doi: 10.1103/PhysRevB.84.035207
- [23] B.E. Sernelius, K.-F. Berggren, Z.-C. Jin, I. Hamberg, C.G. Granqvist, Band-gap tailoring of ZnO by means of heavy Al doping, *Phys. Rev. B* 37 (1988) 10244–10248, <http://dx.doi.org/10.1103/PhysRevB.37.10244>.
- [24] J. G. Lu, Z. Z. Ye, Y. J. Zeng, L. P. Zhu, L. Wang, J. Yuan, B. H. Zhao, Q. L. Liang, Structural, optical, and electrical properties of (Zn,Al)O films over a wide range of compositions, *J. Appl. Phys.* 100 (2006) 073714, doi: 10.1063/1.2357638
- [25] E. O. Filatova, A. S. Konashuk, Interpretation of the Changing the Band Gap of  $\text{Al}_2\text{O}_3$  Depending on Its Crystalline Form: Connection with Different Local Symmetries, *J. Phys. Chem. C* 119 (2015) 20775-20761
- [26] I. Costina, R. Franchy, Band gap of amorphous and well-ordered  $\text{Al}_2\text{O}_3$  on  $\text{Ni}_3\text{Al}$  (100), *Appl. Phys. Lett.* 78 (2001) 4139-4141
- [27] S. K. Sampath, J. F. Cordaro, Optical Properties of Zinc Aluminate, Zinc Gallate, and Zinc Aluminogallate Spinel, *J. Am. Ceram. Soc.* 81 (1998) 649–54

- [28] A.V. Belyaev, I.I. Evdokimov, V.V. Drobotenko, A.A. Sorokin, A new approach to producing transparent  $\text{ZnAl}_2\text{O}_4$  ceramics, *J. Eur. Ceram. Soc.* 37 (2017) 2747–2751, doi: <https://dx.doi.org/10.1016/j.jeurceramsoc.2017.02.041>
- [29] S. Sommer, E. D. Bøjesen, A. B. Blichfeld, B. B. Iversen, Tailoring band gap and thermal diffusivity of nanostructured phase-pure  $\text{ZnAl}_2\text{O}_4$  by direct spark plasma sintering synthesis, *J. Solid State Chem.* 256 (2017) 45-52, doi: <http://dx.doi.org/10.1016/j.jssc.2017.08.023>
- [30] D-Y. Cho, J. H. Kim, K. D. Na, J. Song, C. S. Hwang, B-G Park, J-Y. Kim, C-H. Min, S-J. Oh, Spectroscopic evidence for limited carrier hopping in amorphous ZnO thin films, *Appl. Phys. Lett.* 95 (2009) 261903
- [31] T. Mizoguchi, *J. Phys.: Condens. Matter*, Overlap population diagram for ELNES and XANES: peak assignment and interpretation 21 (2009) 104215
- [32] Y. Imai, A. Watanabe, Comparison of electronic structures of doped ZnO by various impurity elements calculated by a first-principle pseudopotential method, *J. Mater. Sci. : Mater. Electron.* 15 (2004) 743
- [33] C. Wang, Y. Wang, G. Zhang, C. Peng, G. Yang, Theoretical investigation of the effects of doping on the electronic structure and thermoelectric properties of ZnO nanowires, *Phys. Chem. Chem. Phys.* 16 (2014) 3771
- [34] J.A. van Bokhoven, T. Nabi, H. Sambe, D.E. Ramaker, D.C. Koningsberger, Interpretation of The Al K and LII/III edges of aluminum oxides: differences between tetrahedral and octahedral Al explained by different local symmetries, *J. Phys. Condens. Matter* 13 (2001) 10247-10260